Correspondence to:
A. S. J. Khayat,
alain.khayat@nasa.gov

The Mars Atmosphere Water Ice Aerosol Climatology by MRO/CRISM: 5 Mars Years of Observations

Alain S. J. Khayat[1] , **Michael D. Smith[1]** , **Michael J. Wolff[2]** , **Scott D. Guzewich[1]** , **Emily L. Mason[1,3]** , **and Samuel Atwood[4,5]**

[1]Solar System Exploration Division, Planetary Systems Laboratory, NASA Goddard Space Flight Center, Greenbelt, MD, USA, [2]Space Science Institute, Boulder, CO, USA, [3]Center for Space Sciences and Technology (CSST), University of Maryland Baltimore County, Baltimore, MD, USA, [4]Laboratory for Atmospheric and Space Physics, University of Colorado Boulder, Boulder, CO, USA, [5]Department of Earth Sciences, Space and Planetary Science Center, Khalifa University, Abu Dhabi, UAE

Abstract We use near-infrared spectra returned from the Compact Reconnaissance Imaging Spectrometer for Mars (CRISM) aboard the Mars Reconnaissance Orbiter (MRO) to provide retrievals of the column-integrated optical depth of water ice aerosols for more than 5 Martian years between Mars Year (MY) 28 at $L_s = 112°$ (27 September 2006) and MY 33 at $L_s = 213°$ (30 August 2016). We have developed a radiative transfer model for this purpose that retrieves aerosol opacity from the water ice aerosol feature near 3.3 μm using CRISM hyperspectral observations for the first time. The resulting retrievals well depict the main features in the water ice aerosol climatology with repeatable patterns every Martian year. The aphelion cloud belt (ACB) is observed between 10°S and 30°N, with peak optical depth around $L_s = 90°$. Apart from the global dust storm during MY 28, modest interannual variability in the water ice aerosol optical depth is observed in the ACB. The north polar hood is observed at latitudes poleward of 45°N throughout northern spring and summer seasons and reappears in northern winter. The south polar hood is observed in early to mid-southern autumn, reaching latitudes around 60°S, and re-emerging during southern winter between 45°S and 60°S. A lack of water ice aerosols is repeatedly seen in the southern hemisphere throughout southern spring and summer. High optical depth in the ACB is observed over the volcanoes of Olympus Mons, Elysium, and the Tharsis bulge, as well as over Hellas Basin.

Plain Language Summary The atmosphere of Mars can hold water ice crystals when the right temperature and pressure conditions are met. We use observations from an instrument onboard the Mars Reconnaissance Orbiter to track the presence and evolution of water ice in the atmosphere based on how much the ice crystals absorb and scatter sunlight. The observations extend for 5 Martian years (∼10 Earth years) and cover all the Martian seasons. We show that there is a concentration of clouds around the equator of the planet, forming during spring and summer seasons, particularly over the volcanoes on Mars. Water ice clouds are also observed at high latitudes near the poles in the form of polar hoods, showing up in the north during northern spring, summer and winter, and in the south during southern autumn and winter. The main features in the retrieved cloud climatology in this study are repeated every Martian year. The amount of absorption caused by the water ice clouds is similar between the equatorial cloud belt, the north and south polar hoods.

1. Introduction

Water vapor in the Martian atmosphere can condense into ice-crystals under certain conditions, forming water ice clouds that play an important role in the global transport of water. These clouds work as a cooling mechanism by reflecting incoming solar radiation back into space but also as a warming mechanism by absorbing outgoing longwave radiation from the surface of the planet (e.g., Madeleine et al., 2012; Montmessin et al., 2004). The Mariner 9 orbiter presented the first direct spectral evidence of the cloud composition over the Tharsis volcanoes (Curran et al., 1973) by examining the broad features of atmospheric water ice using the thermal infrared interferometer spectrometer (IRIS). Water ice clouds have been characterized ever since using a considerable number of instruments carried by spacecraft and Earth-based observatories. A summary of these observations and analyses can be found in the review paper by Clancy et al. (2017).

To capture the global picture of the state of the Martian atmosphere, the Mars Global Surveyor (MGS) carried the Thermal Emission Spectrometer (TES; Christensen et al., 2001), which recorded infrared spectra of the surface

and atmosphere of Mars between 200 and 1,600 cm^{-1} (6–50 μm) from nadir observations at ∼2:00 and 14:00 local time. The strong and distinct spectral features allowed the retrieval of atmospheric water vapor abundance, water ice and dust aerosol optical depths as well as surface and atmospheric temperatures in the lower atmosphere of Mars up to ∼40 km. Smith et al. (2001) presented zonally averaged water ice optical depth (825 cm^{-1}, ∼12 μm) results from TES for over a full Mars Year (MY) between L_s = 104° (MY 24) and 155° (MY 25). The perihelion season (L_s = 180°–360°) was shown to be relatively dusty and characterized by a cloud-free atmosphere, whereas the aphelion season (L_s = 0°–180°) was cloudy but relatively free of dust. In particular, the zonally averaged climatology indicated the presence of a low latitude belt of water ice clouds between 10°S and 30°N, also known as the aphelion cloud belt (ACB), which spanned L_s = 40°–145° in the aphelion season when the atmosphere is relatively cold, before disappearing after L_s = 145°. The north polar hood was clearly observed during late northern summer around L_s = 160° at mid northern latitudes, and it lasted for the rest of the Martian year. A less prominent polar hood was detected in the south during southern autumn and winter (L_s = 0°–180°) at mid southern latitudes (see Figure 1 in Smith et al., 2001). Subsequent observations from TES extended the water ice cloud climatology for 3 Martian years between MY 24 (L_s = 104°) and MY 27 (L_s = 81°), and the seasonal variability was generally repeated (Smith, 2004). TES thermal infrared retrievals showed that the ACB was prominent at all longitudes, with increased optical depth over the high topographic features due to orographic clouds that form over Elysium and Tharsis. The north polar hood was seen during northern autumn and winter, and it remained until the end of northern spring (L_s = 90°). The south polar hood was also observed from southern autumn (L_s = 0°) to late southern winter (L_s = 150°), with a lack of water ice clouds around L_s = 90° because of the low abundances in water vapor (<5 pr-μm) at high southern latitudes.

Retrievals by Smith et al. (2022) and Atwood et al. (2022) using spectra taken by the Emirates Mars Infrared Spectrometer (EMIRS; Edwards et al., 2021) onboard the Emirates Mars Mission (EMM; Almatroushi et al., 2021; Amiri et al., 2022), are prolonging the multi-decade atmospheric record of water vapor, water ice and dust aerosol optical depths as well as surface and atmospheric temperatures in the lower atmosphere of Mars. Seasonal and latitudinal variations of the water ice column total optical depth at 825 cm^{-1} (∼12 μm) were provided almost continuously during MY 36 from the beginning of the science phase at L_s ∼ 49° to L_s = 180° and showed agreement with previous results by TES.

The Mars Color Imager (MARCI; Malin et al., 2008) onboard the Mars Reconnaissance Orbiter (MRO; Zurek & Smrekar, 2007) has been used to produce daily global maps of the column-integrated water ice optical depth at UV wavelengths using its sensitivity to the contrast between water ice aerosols and the contribution from the surface. By analyzing MARCI/UV images of the surface and atmosphere of Mars taken around 320 nm (Band 7), Wolff et al. (2019) characterized the spatial and temporal evolution of atmospheric water ice aerosols for 6 Martian years between MY 28 (L_s = 153°) and MY 34 (L_s = 178°). Pixels inside the cap on Mars, suspected of potentially including ice, were flagged out using an empirical formulation where the notional cap edges were specified.

The seasonal and latitudinal variation of water ice optical depth for a zonal average and a local time range 14:00–16:00 indicated a repeatable structure from one Martian year to the other with respect to the ACB and the boundaries of the polar hood (see Figure 11 in Wolff et al., 2019). Using a multi-year zonal map, the ACB showed a strong seasonal extent between L_s = 90° and 165° and a geographic extent between 10°S and 30°N. As stated in the study, most of the polar clouds were excluded from the retrievals due to the surface ice flags. However, at the time when the polar hoods were detected, the northern hood was observed between L_s = 180° and 360°, and it lasted to the following year until L_s = 90°. The south polar hood was observed between L_s = 0 and 80°, reaching latitudes as high as 45°S, and latitudes around 40°S at L_s ∼ 110° before moving poleward to 80°S around L_s = 270°.

Nadir spectra recorded in the ultraviolet by the Spectroscopy for Investigation of Characteristics of the Atmosphere of Mars (SPICAM; Bertaux et al., 2006) instrument onboard Mars Express provided the cloud optical depth for SPICAM's first 4 Martian years between L_s = 341° in MY 26 and the end of MY 30 (Willame et al., 2017). The spectral retrieval was performed on 8 separate wavelengths between 220 and 290 nm away from major atmospheric CO$_2$ absorptions and calibration inaccuracies. The team excluded retrievals over surface ice in the polar caps by predicting the presence of surface ice using the Mars Climate Database (MCD, version 5.0; Millour et al., 2012), and treated regions at the edge of the ice caps as "uncertain" (see Retrieval method in Willame et al., 2017). Seasonal and zonally averaged maps of cloud opacity were presented, showing two fundamental

cloud features, the ACB and the polar hoods, repeated every Martian year. During the aphelion season, the ACB begins to form in the $L_s = 20°–30°$ period at equatorial latitudes, reaching a maximum extent and intensity by encircling the equator between $L_s = 80°$ and $140°$ with the highest optical depth over elevated regions such as the Tharsis ridge, Olympus and Elysium Mons, before gradually dissipating in later seasons, except for the clouds hovering above the volcanoes in Arsia Mons (10°S–120°W) around perihelion. The north polar hood developed over the poles and was well observed between $L_s = 90°$ and $200°$ during MY 27 poleward of 45°N latitude, and its edges were still visible in the $L_s = 330°–350°$ range during MY 27 and 29 at 45°N–60°N. Parts of the south polar hood were observed every Martian year between $L_s = 0°$ and $L_s = 60°$, and during MY 27 and 29 between $L_s = 120°$ and $L_s = 200°$ where the retrievals of cloud optical depth were made possible.

By fitting portions of the spectra recorded by the Observatoire pour la Minéralogie, l'Eau, les Glaces et l'Activité (OMEGA) instrument aboard Mars Express at near-infrared wavelengths between 1.18 and 3.52 μm, Olsen et al. (2021) were able to derive the physical properties of water ice clouds for a subset of OMEGA's spectral images. The subset includes 94 cloudy OMEGA observations that overlap with 60 cloud-free surface albedo maps from a previous work by Geminale et al. (2015), taken between 35°S and 35°N, and between 140°W and 90°E during the aphelion period ($L_s = 35°–135°$) from three Martian years (MY 27–29). Following the technique developed by Madeleine et al. (2012), Olsen et al. (2021) retrieved the water ice aerosol optical depth at 0.67 μm, and used these properties to estimate the water ice column (WIC; pr-μm) and formulate an empirical relationship between the WIC and the "ice cloud index" (ICI), defined as the ratio between the reflectances at 3.40 and 3.52 μm in the water ice's spectral feature. This statistical approach was later used to estimate the WIC and provide insights into the daytime climatology of water ice between MY 26 and MY 32. The ACB was clearly seen around the equatorial latitudes and centered around $L_s = 90°$, and enhancements in the total water ice column were observed in the north polar hood between $L_s = 130°$ and $L_s = 100°$ of the following year and in the south polar hood between $L_s = 140°$ and $L_s = 200°$.

Using solar occultation observations by the mid-infrared channel of the atmospheric chemistry suite (ACS) instrument onboard the ExoMars Trace Gas Orbiter (TGO), Stcherbinine et al. (2022) monitored the presence of water ice clouds for two Martian years between the beginning of the ACS observations at $L_s = 163°$ in MY 34 and $L_s = 181°$ in MY 36. The retrieved vertical distribution indicated that the typical altitude of water ice clouds varies by 20–40 km between summer and winter, and the clouds are also found to be 20–40 km higher around the equator compared to polar regions. Fedorova et al. (2020) used ACS to characterize the vertical distribution and saturation of water during the 2018 global dust storm and concluded that water access to high-altitude is preferentially occurring close to perihelion, which may have controlled the loss of water from Mars' atmosphere. Concurrent solar occultation observations taken by the Nadir and Occultation for MArs Discovery (NOMAD) instrument aboard TGO covered the period from $L_s = 162°$ of MY 34 to $L_s = 15°$ of MY 35, which also included the 2018 global dust storm. The NOMAD retrievals by Liuzzi et al. (2020) of the vertical distribution of water ice aerosols indicated the presence of a rapid lifting of mesospheric water ice clouds from 45 to 80 km in altitude in a matter of days due to the heating of the lower atmosphere during the storm.

In this study, we provide retrievals of the column-integrated water ice optical depth in the atmosphere of Mars using for the first time hyperspectral observations taken by the Compact Reconnaissance Imaging Spectrometer for Mars (CRISM). This climatology reaches polar regions excluded from previous works, and it covers the entire lifetime of CRISM's near infrared observations, which include the 5+ Martian years between MY 28 at $L_s = 112°$ (27 September 2006) and MY 33 at $L_s = 213°$ (30 August 2016), providing a valuable contribution to the existing water ice climatology provided by other instruments aboard Mars-orbiting spacecrafts.

In Section 2, we provide information on the CRISM instrument, the observing mode and the data used in this study. In Section 3, we detail the retrieval process and the arising uncertainties, the surface ice flags and present a showcase of retrievals over the polar regions. In Section 4, we present the CRISM climatology of water ice aerosol optical depth and compare it with retrievals by THEMIS, discuss the interannual variations and provide the geographic enhancement in water ice aerosol optical depth in the ACB, particularly over volcanic districts. We summarize this work in Section 5.

2. Data Set

2.1. CRISM Instrument and Observations

The CRISM instrument is a hyperspectral imager onboard MRO, capable of observing the atmosphere in the limb viewing mode using a gimbal, as well as the surface and atmosphere simultaneously at the nominal nadir pointing
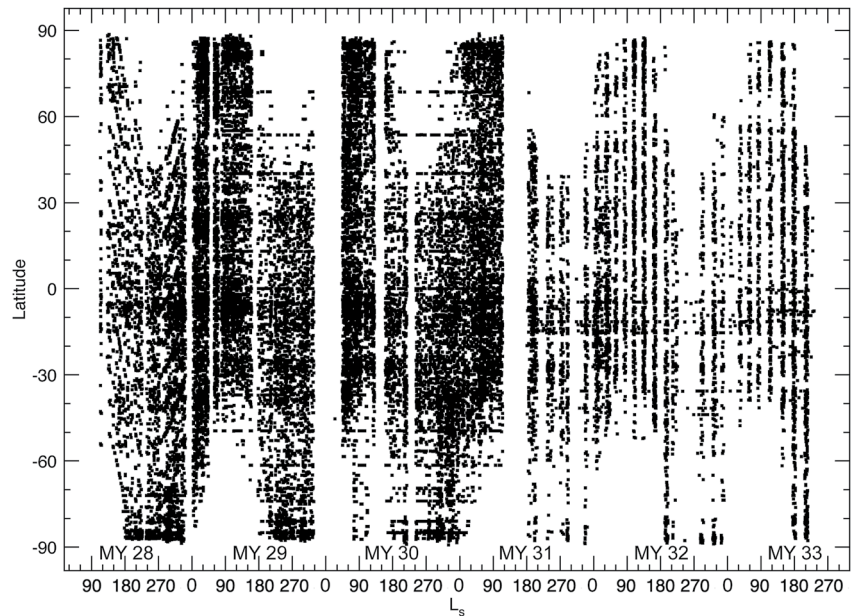
Figure 1. Distribution of the Compact Reconnaissance Imaging Spectrometer for Mars (CRISM) observations as a function of season (L_s) and latitude used in this work to retrieve the water ice aerosol optical depth. The observations extend for over 5 Martian years (Mars Year 28–33) and the diminishing frequency in observations at the end is caused by the team choosing to take fewer near-infrared observations in order to preserve the lifetime of CRISM's degrading cryocooler. Other gaps in observations are due to solar conjunctions and spacecraft anomalies.

mode (Murchie et al., 2007). At the hyperspectral setting, the instrument takes advantage of its 545 channels covering visible and near infrared wavelengths between 362 and 3,290 nm at an average spectral resolving power of 150. The wavelength coverage and resolution has allowed the retrieval of the main atmospheric constituents such as carbon dioxide (CO_2), water vapor (H_2O), and carbon monoxide (CO) from nadir observations (e.g., Khayat, Smith, & Guzewich, 2019; Khayat et al., 2020, 2022; Smith et al., 2009, 2018, 2022; Toigo et al., 2013), the vertical distribution of Martian aerosol (Smith et al., 2013) and their particle size (Guzewich & Smith, 2019; Guzewich et al., 2014), as well as the O_2 singlet delta emission (Clancy et al., 2012, 2013) from limb-geometry observations.

Due to the spacecraft's sun-synchronous orbit, the daytime nadir observations were always conducted at ~15:00 hr local time, with a spatial resolution as good as 20 m/pixel in the fully resolved targeted mode. However, we are interested in atmospheric phenomena larger than the pixel size; therefore, we bin the central 100×100 pixels of every hyperspectral observation at nadir to conduct the water ice optical depth retrievals, which corresponds to a footprint of ~2×2 km. This spatial averaging enhances the signal-to-noise ratio by a factor between 2 and 3 depending on the observation, but the presence of systematic uncertainties does not necessarily allow further improvement in the signal-to-noise ratio, as also observed and noted in Smith (2009).

The ~27,300 observations used here were taken during the primary science phase, which began at MY 28 at $L_s = 112°$ (27 September 2006), and they extend for more than 5 Martian years until MY 33 at $L_s = 213°$ (30 August 2016), beyond which a degradation in the instrument's cryocooler limited the near-infrared sensitivity and led to the eventual end of near-infrared observations. However, the existing coverage is more than sufficient to characterize the water ice aerosol climatology. Figure 1 shows the distribution of the hyperspectral observations used in this work as a function of season and latitude for the entire lifetime of CRISM, providing a window into the seasonal, spatial and interannual variations of water ice aerosols in the Martian atmosphere, with a climatology of water ice for more than 5 Martian years. CRISM spectra capture signatures from the surface and atmosphere of Mars in the solar reflected regime, and therefore cannot observe regions on Mars that are not illuminated, hence the gaps in coverage during polar nights in Figure 1.

Figure 2 shows a near-nadir CRISM spectrum in the wavelength range of interest. The ratioed spectrum (I/F) is the ratio of the radiance measured by CRISM's detector (I) to the solar irradiance (F) at the top of the Martian
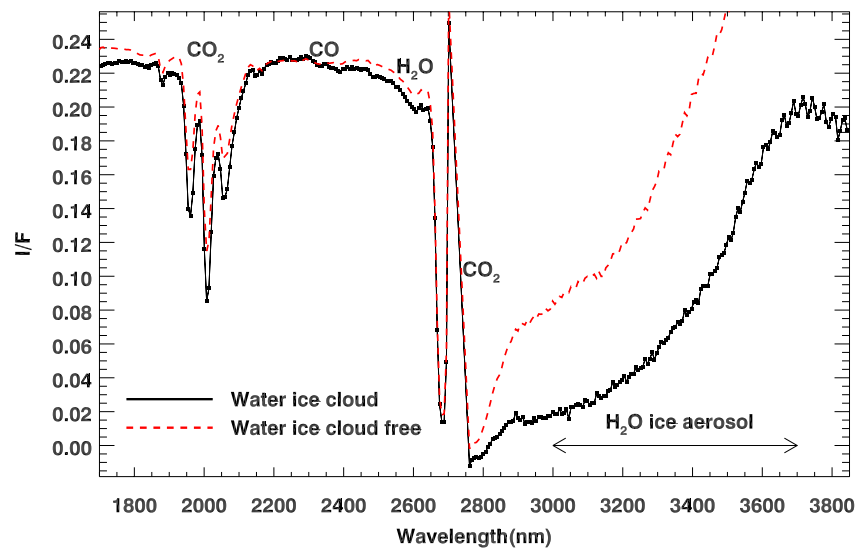
Figure 2. An example of a portion of the near-nadir Compact Reconnaissance Imaging Spectrometer for Mars spectrum (solid black) from observation EPF0000BD4B taken in July 2008 at $L_s = 105°$ (MY 29), and centered at 21.56°N latitude, 16.15°W longitude. The absorption bands from CO_2, H_2O, and CO are indicated, and the large water ice aerosol feature is detected in the 3,000–3,700 nm range. The reflectances at 3,380 and 3,520 nm are used to calculate the water ice opacity index. In comparison, the normalized dashed red spectrum corresponds to cloud-free observation EPF000054C1 taken at $L_s = 217°$ (MY 28) and centered at 21.46°S latitude and 52.71°W longitude.

atmosphere. The main absorption bands are present at 2.0 and 2.75 μm for CO_2, 2.6 μm for H_2O, and a weak band of CO is present around 2.35 μm. The water ice aerosol absorption feature of interest exists between 3.0 and 3.7 μm, away from the regions of high gas absorption, and we rely on this band to retrieve the total water ice optical depth in this study.

2.2. Water Ice Aerosol Opacity Index

As a first order metric to identify the presence of water ice clouds, a water ice opacity index is defined as $IOI = 1 − (I/F)_{3.38 \, \mu m}/(I/F)_{3.52 \, \mu m}$, where I/F are the reflectances at 3.38 and 3.52 μm, and it corresponds to the reversed ice cloud index (ICIR) defined in Szantai et al. (2021). The index represents the slope in the water ice feature, and a higher IOI is indicative of denser/thicker/more frequent clouds, with a minimum threshold for cloud ice identification set to 0.28 (Langevin et al., 2007; Olsen et al., 2021; Szantai et al., 2021). This threshold is more stringent than the adopted 0.2 by Madeleine et al. (2012), and so now excludes thin clouds (Szantai et al., 2021). We computed the IOI using 5 MYs of CRISM hyperspectral observations and combined the results to map the seasonal dependence of the water ice aerosol index as shown in Figure 3. The results clearly depict the atmospheric water ice column climatology on Mars as described by previous work (e.g., Clancy et al., 2017 and references therein). The ACB is clearly observed between $L_s = 80°$ and 130° between 10°S and 30°N. The north polar hood is present during north autumn and winter ($L_s = 180°–360°$) and remains present until early northern summer ($L_s = 90°$) of the following year. The south polar hood is present throughout southern autumn and winter ($L_s = 0°–180°$). In this work, we apply a full radiative transfer model to the entire CRISM hyperspectral data set in order to retrieve the total column water ice aerosol optical depth.

3. Method

3.1. Retrieval Process

The retrieval algorithm here is a modified version of that first introduced by Smith et al. (2009), and used by Smith et al. (2018) to retrieve atmospheric water vapor and carbon monoxide using the same CRISM observations in this study. The retrieval process was extensively explained in Smith et al. (2009) and we provide information on the current modifications to the retrieval algorithm targeting the water ice aerosol feature. The retrieval of the water ice optical depth is conducted in spectral regions devoid of significant contamination belonging to
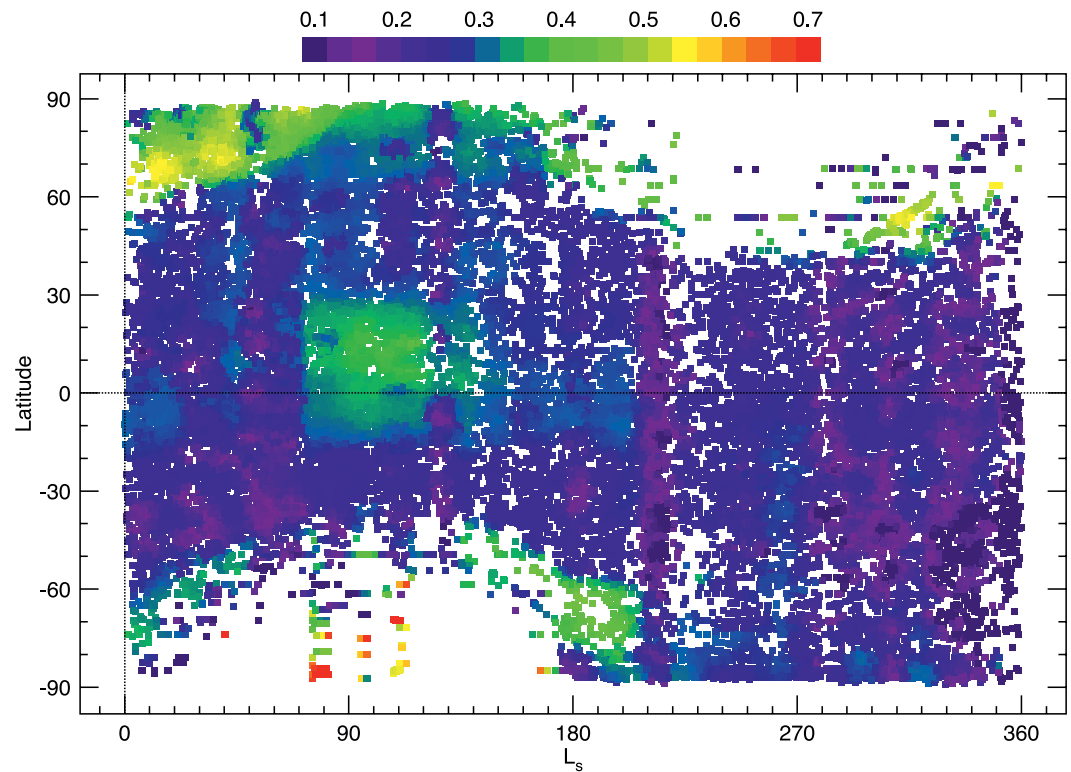
Figure 3. The seasonal dependence of the atmospheric water ice aerosol opacity index around 3.4 μm using the Compact Reconnaissance Imaging Spectrometer for Mars hyperspectral observations. The index is a metric of the aerosol band depth and is unitless, where a higher index indicates thicker/denser/more frequent water ice clouds. As observed, the annual cycle of water ice clouds with its distinctive aphelion cloud belt, north and south polar hoods is well depicted here.

molecular absorptions from atmospheric CO_2, H_2O or CO. The radiation collected by CRISM is largely solar radiation being reflected from the surface and absorbed and scattered by the atmosphere of Mars into the line of sight (e.g., Khayat, Villanueva, et al., 2019; Smith et al., 2013). The radiative transfer including scattering by atmospheric aerosols is modeled using the discrete ordinates method described in Thomas and Stamnes (1999) and we adopt a spherical shape for the water ice aerosols, as in Smith et al. (2018). The wavelength-dependent aerosol scattering properties are obtained from Wolff et al. (2009), who used CRISM observations of a fixed spot on the Martian surface at various emission angles. To be consistent with previous works (e.g., Khayat, Smith, & Guzewich, 2019; Smith et al., 2009, 2013, 2018), we adopt effective radii (r_{eff}) of 2.0 and 1.5 μm for ice and dust aerosol particles, respectively. The particle sizes were derived from synthesizing spectra returned by the TES (Wolff & Clancy, 2003) and by comparing them against mini-TES and CRISM spectra (Clancy et al., 2003; Wolff et al., 2006, 2009). We present in Figure 4 the extinction coefficient (Q_{eff}) and the single scattering albedo (ϖ) for water ice aerosols used here to retrieve the total column optical depth. The geometrical quantities used in the radiative transfer model, including the emission angle (where observations with emission angles >30° are excluded), the solar incidence angle (where observations with incidence angles >80° are excluded), and the distance between Mars and the Sun at the time of the observation, are all taken from spacecraft records. The solar radiance adjusted at Mars distance is based on the MODTRAN-modeled solar spectrum (Berk et al., 1998).

Observations by the Thermal Emission Imaging System THEMIS (Smith et al., 2003) on Mars Odyssey allowed the retrieval of the water ice and dust aerosol absorption optical depths. The extinction (scattering + absorption) optical depths at the CRISM wavelengths for dust and water ice aerosols are respectively ∼1.3 and 1.5 times absorption optical depths retrieved by THEMIS (Smith, 2004) and are further scaled between THEMIS (12 μm) and CRISM (3.3 μm) wavelengths. The scaled dust optical depth and the a priori water ice optical depth used here in our CRISM retrieval originate from the concurrent THEMIS retrievals.

The retrieval process is iterative, and in order to establish the contrast between the continuum level and the water ice aerosol feature and determine the water ice optical depth, we first fit the effective Lambert surface albedo at
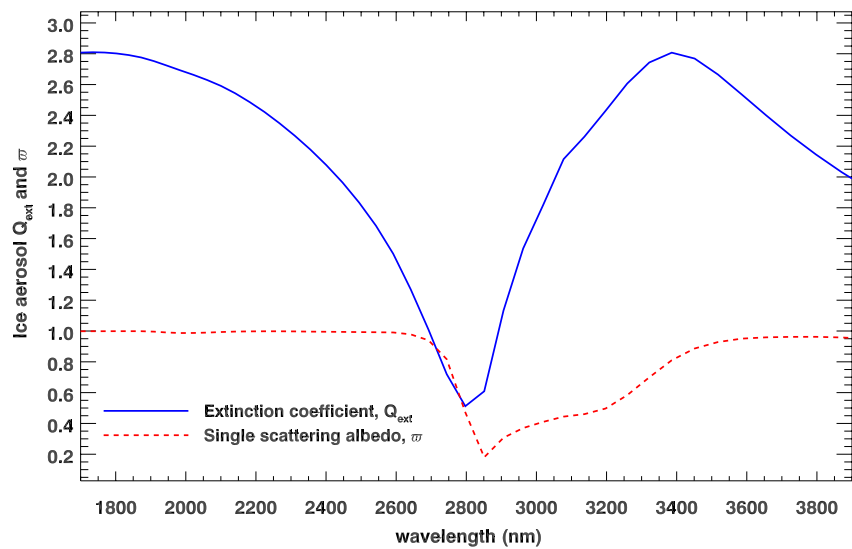
Figure 4. The water ice aerosol extinction coefficient (Q_{ext}) and the single scattering albedo (ϖ) as a function of wavelength for the representative mean particle size $r_{\text{eff}} = 2$ μm used in this work.

three wavelengths at 2.9, 3.5, and 3.6 μm, and then linearly interpolate the Lambert surface albedo in between those wavelengths. The wavelengths are chosen away from major atmospheric gas features and in spectral regions affected by surface albedo and atmospheric aerosols. In the second step, we model the water ice aerosol feature using a total of 8 spectral channels in the CRISM spectrum (2.900, 2.999, 3.098, 3.198, 3.297, 3.397, 3.497, and 3.600 μm), and we vary the water ice aerosol optical depth until a best fit is achieved between the synthesized and the observed spectrum, using the Levenberg-Marquardt nonlinear minimization technique (Press et al., 1992). The use of 8 spectral channels to complete the spectral fitting procedure is a tradeoff between accuracy and computer efficiency. Even though the surface albedo is retrieved around the same spectral interval covered by the water ice aerosol feature, the surface albedo is responsible for the linear continuum level below which the curved "bowl shaped" water ice feature lies, where the feature's depth is proportional to its optical depth. The output quantities from the retrieval process are the surface Lambert Albedo at three wavelengths (2.9, 3.5, and 3.6 μm) inside the water ice feature and the column-integrated water ice aerosol optical depth at ~3.3 μm. In Figure 5 we present the result from fitting a synthetic spectrum to the observed CRISM observation EPF0000BD4B (shown previously in Figure 2). We retrieve a water ice aerosol optical depth of 0.28, indicating the presence of water ice clouds as expected during the aphelion season at which the observation was taken.

3.2. Retrieval Uncertainties

The retrieval algorithm here is a modified version of the one described in Smith et al. (2009, 2018) and it targets water ice aerosols instead of gas abundances (e.g., Khayat, Smith, & Guzewich, 2019; Khayat et al., 2020, 2022), and so there are slight differences in the evaluation of uncertainties. In a similar fashion, the uncertainties are determined by perturbing the input parameters in the radiative transfer model and then measuring the resulting change in the output quantities. We apply the numerical experimentation to the typical observation EPF0000BD4B shown in Figures 2 and 5 and estimate the uncertainties as follows.

CRISM's optical configuration induces a wavelength offset that increases away from the center of the observation; therefore, we use the central 100×100 pixels (or "sweet spot") of each observation to minimize the effect of the wavelength offset. However, the offset could still reach a maximum of 3 nm (see Figure 3 in Khayat et al., 2022), and previous works (e.g., Smith et al., 2009) relied on the strong CO_2 absorption band to measure and correct the offset within the sweet spot, a necessary step when retrieving weak or narrow bands of molecular species in the Martian atmosphere. In this work, we rely on the broad water ice aerosol feature around 3.3 μm, and we do not use the CO_2 absorption band to retrieve the wavelength offset. We studied the effect of a wavelength offset of a maximum value of 3 nm and found a change that is less than 1% in the retrieved water ice optical depth.

Another assumption is the use of the THEMIS climatology for dust aerosol optical depth in our retrievals after converting the absorption optical depth in the thermal infrared to total extinction optical depth in CRISM's near
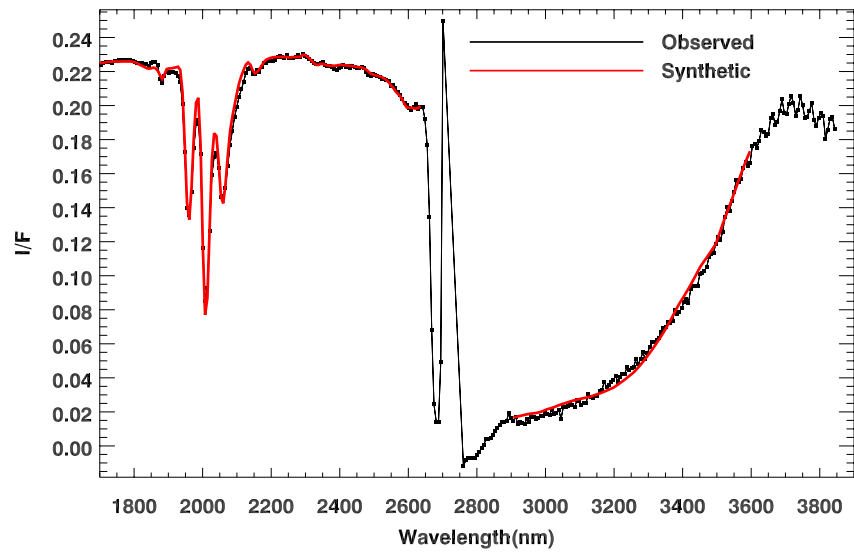
Figure 5. The portion of the Compact Reconnaissance Imaging Spectrometer for Mars (CRISM) spectrum of EPF0000BD4B as observed at equatorial latitudes. The best fit spectrum (red) of the atmospheric water ice aerosol feature using eight channels between 3,000 and 3,603 nm is compared against the CRISM observation (black) taken during the aphelion season. The retrieved value for the water ice aerosol column optical depth is 0.28, indicating the presence of water ice clouds as part of the aphelion cloud belt.

infrared regime. In nominal non-dust storm condition, setting the optical depth of dust to zero, or doubling it induces a maximum change of 1% in the retrieved water ice optical depth. In a dust storm scenario, the dust optical depth exceeds unity, resulting in a maximum change of 50% in the retrieved water ice optical depth. However, in realistic dust storm scenarios, the atmosphere is too warm to hold water ice aerosols, and the water ice optical depth would be very low during dusty seasons (e.g., Smith, 2009).

Aside from the temperature-dependent broadening of the CO_2 band in the CRISM data and as stated before, the CRISM near infrared spectra are mostly insensitive to atmospheric temperature and instead depend on the solar reflected radiation from the surface and atmosphere of the planet. The vertical temperature profiles are important, however, in controlling molecular spectral line shapes by impacting the broadening coefficients and the spectral line strengths of the molecular species. However, in the current work, we target a wavelength range from 3.0 to 3.7 μm where no major molecular gas absorptions from CO_2, H_2O, and CO are present, so our retrievals are insensitive to the temperature profile. Likewise, the changes in the surface pressure, a metric for the abundance of CO_2, do not impact the water ice aerosol optical depth.

The instrumental noise is relatively small when averaging the central 100×100 pixels in every observation, with an average signal-to-noise ratio of 1,000; however, systematic uncertainties do not necessarily average out and are difficult to evaluate. We find that a change in the radiance level of $\pm 5\%$ (larger than known and expected systematic errors) for the high-signal and low-signal (from dark regions) spectra leads to a maximum change in the retrieved water ice optical depth of 29% and 20%, respectively.

Aerosol scattering related assumptions including the number of streams (16) used in the discrete ordinates, the number of expansion orders (32) in the Legendre polynomials of the scattering phase function, as well as the number of atmospheric levels (25) used in the radiative transfer model can potentially lead to uncertainties in the retrieved water ice aerosol optical depth, but those uncertainties are typically small, on the order of 2% or less.

As a result of the numerical experimentations and the sources of uncertainty, we estimate the total uncertainty in the water ice optical depth to be less than 30%.

In order to test the dependence of the optical depth on the particle size, we performed retrievals over 1,000 random spectra across random longitudes, latitudes and seasons on Mars using water ice aerosol particle sizes of 1.5 and 3.0 μm. Figure 6 shows the retrieved optical depth of water ice aerosols when adopting 2.0 μm particle size in our study compared to 1.5 and 3.0 μm. The optical depth when adopting 1.5 μm is within 20% of the
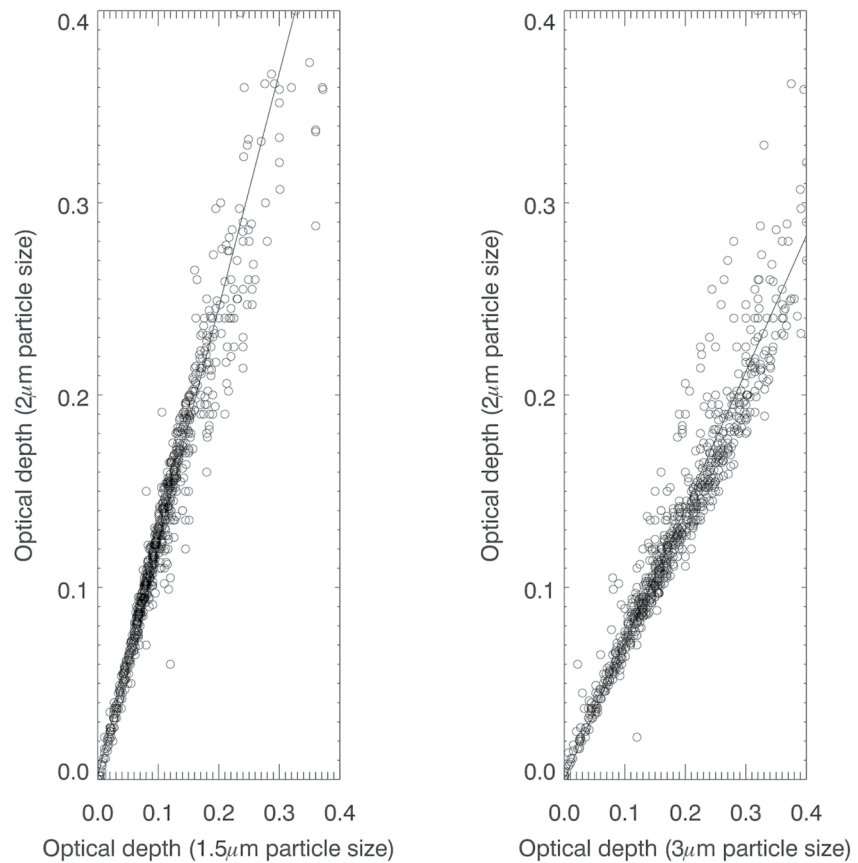
Figure 6. The retrieved optical depth when using 2.0 μm particle size versus 1.5 μm (left) and 3.0 μm (right). The solid line shows the linear fit between the retrieved optical depths.

optical depth when adopting 2.0 μm, and within 30% when adopting 3.0 μm particle size. What is most important here is that the retrieved optical depths are all systematic with a very strong correlation between each other at various particle sizes, therefore conserving the main patterns of the water ice climatology we present in this work, and the conclusions remain unchanged.

3.3. Surface Ice

The solar reflected radiation from the surface of Mars carries spectral information pertaining to the surface properties. In particular, the presence of surface ice over the poles contaminates the spectral features belonging to the atmospheric constituents such as water vapor, carbon dioxide and aerosols. Previous works (e.g., Appéré et al., 2011; Langevin et al., 2007) introduced the surface ice index using Mars Express/OMEGA spectra to develop surface ice maps to track the evolution of the seasonal deposits in the north cap and the recession of the south seasonal cap. In order to provide insights into the distribution of surface ice in the north polar layered deposits, Brown et al. (2016) calculated the depth of the water ice absorption band (hereafter, surface H_2O ice index) in the CRISM spectra at 1.5 μm and associated the presence of water ice on the surface with a threshold index of 0.125 or higher. Khayat, Smith, and Guzewich (2019) provided retrievals of atmospheric water vapor over the north polar region on Mars during spring and summer seasons and implemented a threshold of 0.1 for the presence of water ice on the surface (see their Figure 2).

Langevin et al. (2007) also introduced a surface ice index to identify the CO_2 ice deposits over a large portion of the south polar region. This index is calculated from the CO_2 ice band around 2.344 μm, and we use the same CO_2 surface ice threshold of 0.045 from Khayat, Smith, and Guzewich (2019). Using both thresholds of surface ice indices, we minimize the contamination with surface ice by avoiding retrievals of water ice aerosol optical depth over ice-covered regions, where 11% of all the observations include water ice on the surface, and 6% of the observations include CO_2 ice on the surface.

Journal of Geophysical Research: Planets

3.4. Polar Observations

As a test case for polar observations where we avoid surface ice but still provide retrievals of water ice aerosol optical depth, we apply the water ice aerosol opacity index and the surface H_2O index to CRISM observation HRL0000AA2A taken during northern spring ($L_s = 65°$) over a polar crater at latitude 73.41°N, to track the presence of water ice clouds and surface ice, respectively. Using the water ice aerosol feature around 3.3 μm, the ice opacity index in the observation is shown in Figure 7, panel A, where water ice clouds are concentrated in the form of stripes mostly located around the center of the observation in the middle of the crater, and extending to the northern part of the observation. The distribution of surface ice is shown in panel B of the same figure, indicating the presence of ice at the rim of the crater in the north and south directions, and the absence of surface ice in the center of the crater where the retrieval of water ice aerosol optical depth is performed. Panel C shows the enhanced visible color image, clearly indicating the presence of thick clouds in the form of stripes over the crater, as part of the greater north polar hood. Even though we here show the full extent of the CRISM observation to provide an example of the extent of water ice clouds, we perform in this work the retrievals of the water ice aerosol optical depth over the central 100×100 pixels away from surface ice, as indicated for this particular observation in panel B at the center. The retrieval of the water ice aerosol optical depth returns a value of $\tau_{ice} = 0.27$, and the synthesized spectrum using our retrieval method is shown in panel D of the same figure, overlaying the observed CRISM spectrum. This ability to identify water ice clouds provides reliable retrievals of water ice aerosol optical depth over the polar regions where surface ice is absent.

4. Results and Discussion

The retrieved water ice aerosol climatology from CRISM observations extends for over 5 Martian years between MY 28, $L_s = 112°$ (27 September 2006) and MY 33, $L_s = 213°$ (30 August 2016), resulting in 22,000 successful retrievals. The entire climatology is shown in Figure 8, with a comparison against THEMIS retrievals (Smith, 2019a). The main trends in the water ice aerosol climatology are well depicted in the CRISM retrievals.

As shown in Figure 8 (upper and lower panels), the water ice optical depth gradually increases after the beginning of northern spring ($L_s = 0°$), and it expands away from being centered around the equator. For MY 28, the ACB is observed at the beginning of CRISM's coverage during northern summer at $L_s = 110°$ and it covers the latitudinal range 10°S−30°N. During MY 29, the ACB exhibits a short seasonal and latitudinal extent between $L_s = 60°$ and 130° and latitudes 0°S and 30°N, respectively. This short extent is also observed by OMEGA (Willame et al., 2017), in parallel with elevated amounts of dust (high dust optical depth) detected using the same instrument, which warms up the atmosphere and depresses the formation of water ice clouds. The seasonal coverage of the ACB returns to nominal values in the following Martian years. After a lapse in coverage at the beginning of MY 30, the ACB is observed during early northern spring ($L_s = 0°$–90°) at $L_s = 30°$ between 0°N and 25°N, before extending latitudinally to cover latitudes in the 10°S−30°N range at its maximum around $L_s = 120°$, and dissipating after $L_s = 150°$. In MY 31, the ACB covers the same seasonal and latitudinal ranges as in MY 30 despite a lack in CRISM's coverage occurring at $L_s = 120°$. In MY 32, the cloud belt is observed during northern spring ($L_s = 0°$–90°) and summer ($L_s = 90°$–180°) between $L_s = 30°$ and $L_s = 140°$, with an increasing latitudinal extent reaching its peak at $L_s = 110°$ between 10°S and 30°N, followed by a decay in the latitudinal coverage and a dissipation beyond $L_s = 140°$. This pattern is similarly repeated in MY 33. The ACB does not exhibit any major interannual changes except for MY 29.

The north polar hood, characterized by a high optical depth of water ice aerosols in the northern hemisphere, is observed at latitudes poleward of 45°N repeatedly every Martian year, as shown in Figure 8. During MY 28, the polar hood is present at the beginning of the CRISM observations in early northern summer ($L_s = 90°$–180°) at $L_s = 90°$ at latitudes poleward of 60°N and persists at those latitudes until the end of northern summer ($L_s = 180°$) beyond which retrievals are no longer possible because of the polar night. The north polar hood re-emerges at latitudes around 45°N at the beginning of northern winter ($L_s = 270°$–360°) at $L_s = 270°$ in the same MY 28 and gradually shifts toward higher latitudes during northern spring ($L_s = 0°$–90°) and summer seasons ($L_s = 90°$–180°) of the following MY 29 and lasting until mid-northern autumn ($L_s = 180°$–270°) by covering lower latitudes in the 45°N−60°N range. In MY 30, the north polar hood is observed poleward of 60°N in mid-northern summer ($L_s = 90°$–180°) starting at $L_s = 45°$ due to the gap in coverage by CRISM, and it persists at those latitudes until the mid-northern summer ($L_s = 135°$). As in previous Martian years, the north polar hood reappears during late northern autumn ($L_s = 180°$–270°) at lower latitudes around 45°N, with a higher water ice aerosol optical depth
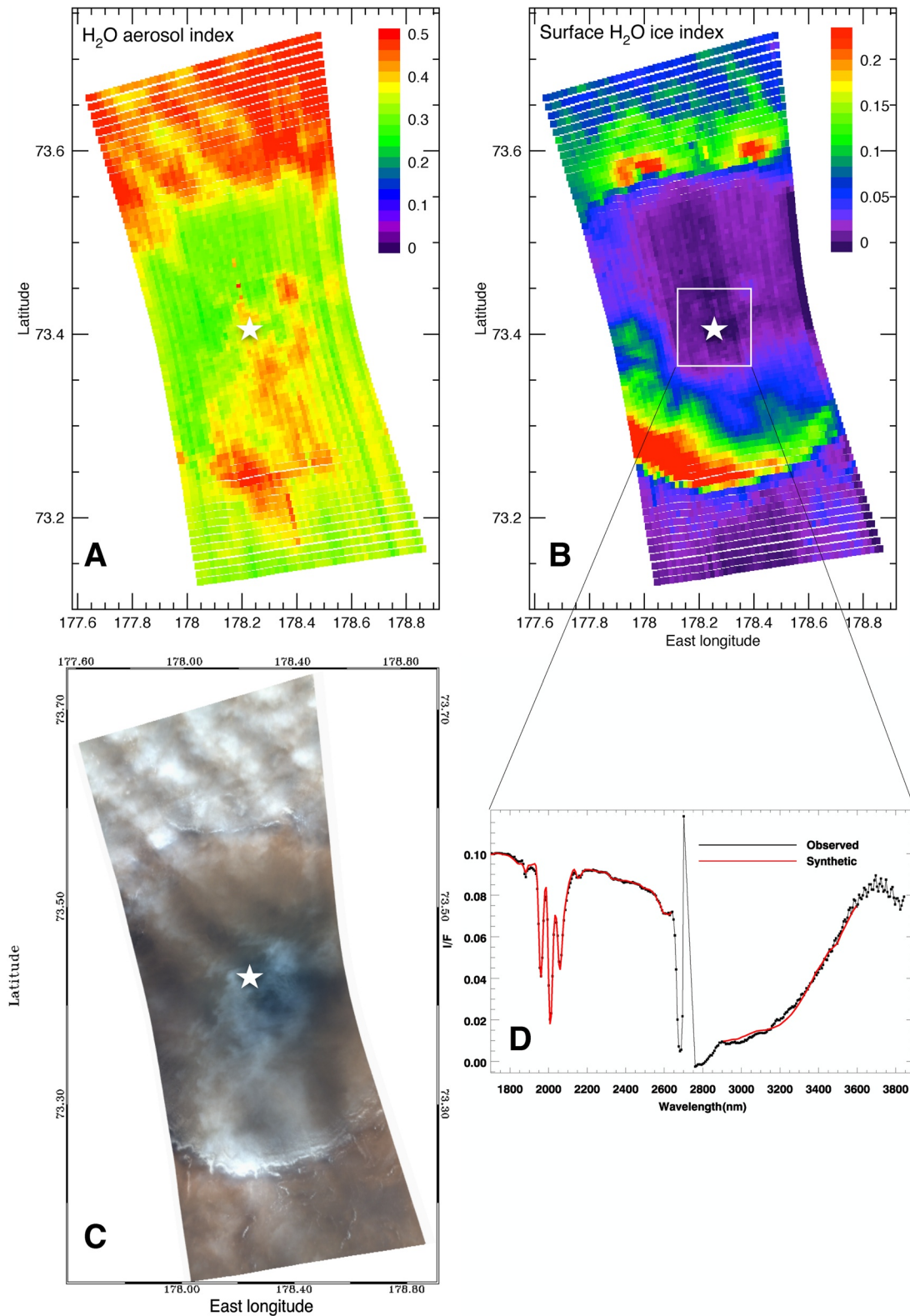
Figure 7. Panel (a) shows the retrieved ice aerosol opacity index (see Section 2.2) for observation HRL0000AA2A, taken on 28 April 2008 during later northern spring and centered at longitude 178.26°E and latitude 73.41°N. Panel (b) shows the surface ice index (see Section 3.3), and panel (c) shows the enhanced visible color image. The square in the middle of panel (b) indicates the central 100×100 pixels from which the coadded spectrum used for the observation is extracted. Panel (d) shows the observed and fitted spectra of the observation in black and red, respectively.

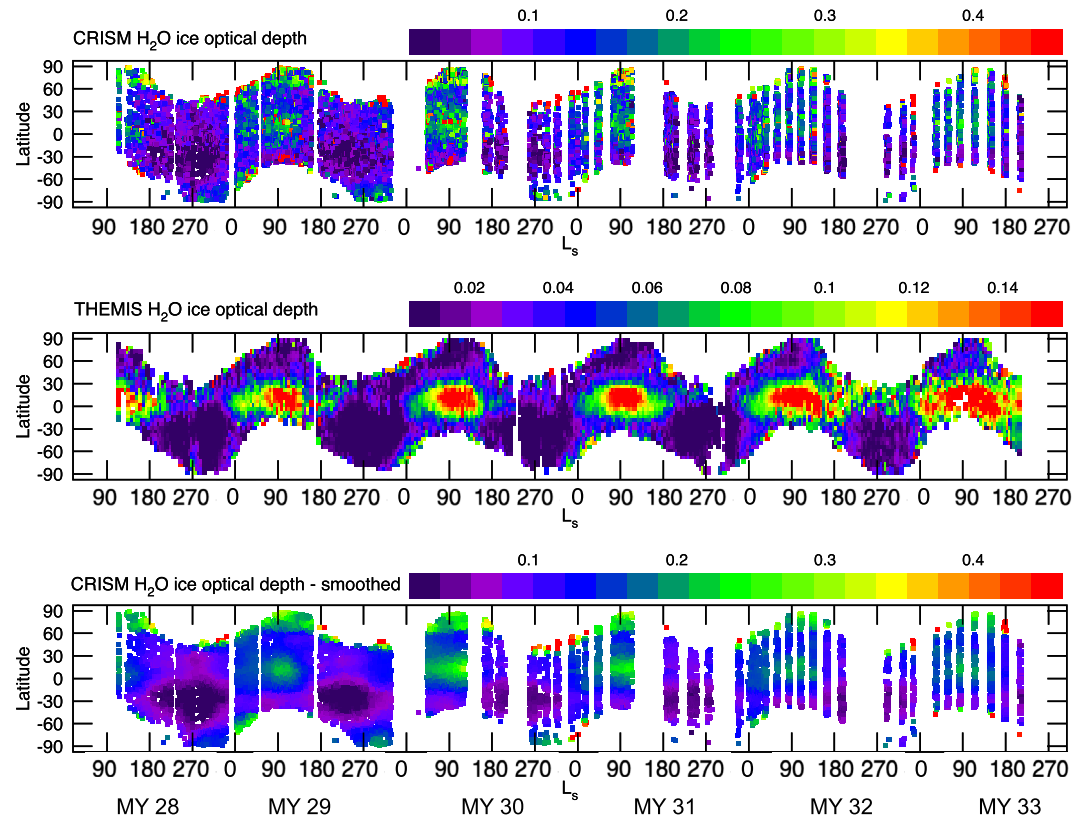**Figure 8.** Zonal average of the water ice aerosol optical depth for over 5 Martian years. (top) Retrieved climatology of the Compact Reconnaissance Imaging Spectrometer for Mars (CRISM) water ice aerosol extinction (scattering and absorption) optical depth at ~3.3 μm as a function of season (L_s) and latitude. (middle) Concurrent THEMIS climatology of the water ice aerosol absorption optical depth at 12.1 μm (825 cm^{-1}). Notice the difference in scale between the two retrievals. (bottom) A smoothed version of the results from the top panel to distinguish the major features in the CRISM water ice aerosol climatology. The Martian year number is indicated by "MY" at the bottom of the figure.

at those latitudes during northern winter ($L_s = 270°$–$360°$), followed by a shift in the latitudinal extent covering higher latitudes in northern spring ($L_s = 0°$–$90°$) and summer ($L_s = 90°$–$180°$) of the following Martian year. During MY 32 and MY 33, the north polar hood follows a similar behavior in its seasonal and spatial coverage compared to the previous Martian years, with no noticeable exceptions.

The increase in water ice optical depth at high latitudes in the southern hemisphere, known as the south polar hood, is observed during the southern winter ($L_s = 90°$–$180°$) of MY 28 between $L_s = 120°$ and $180°$, covering $60°$S latitude around $L_s = 120°$ and moving south toward polar latitudes around $L_s = 180°$, as shown in Figure 8 (upper and lower panels). The south polar hood is also well detected in MY 29 during southern autumn ($L_s = 0°$–$90°$), covering polar latitudes near $L_s = 0°$ and latitudes as low as $60°$S at $L_s = 70°$, as well as low latitudes around $45°$S in the $L_s = 90°$–$120°$ range, before reappearing during southern summer ($L_s = 270°$–$360°$) between $L_s \sim 270°$ and $330°$ at polar latitudes. After a gap in coverage lasting between the end of MY 29 and the beginning of MY 30, the south polar hood is seen again around $60°$S during mid-southern autumn ($L_s = 45°$), around $45°$S at the beginning of southern winter ($L_s = 90°$), and throughout southern summer ($L_s = 270°$–$360°$) at polar latitudes. In MY 31, MY 32 and MY 33, the repeatable pattern where the south polar hood develops at polar latitudes around the beginning of southern autumn ($L_s = 0°$–$90°$) and extends to lower latitudes at ~$60°$S around mid-southern autumn is also clearly observed.

A lack of water ice aerosols is seen mostly in the southern hemisphere throughout southern spring and summer ($L_s = 180°$–$360°$), and it is driven by warming of the atmosphere caused by an increase in the amount of dust during the perihelion season. The lack in water ice aerosols extends over southern latitudes, and its maximum latitudinal coverage occurs between $L_s = 220°$ and $L_s = 270°$ in every Martian year, at latitudes between $0°$S and $60°$S. In MY 28, the lack of water ice clouds also extends to mid-latitudes in the northern hemisphere between
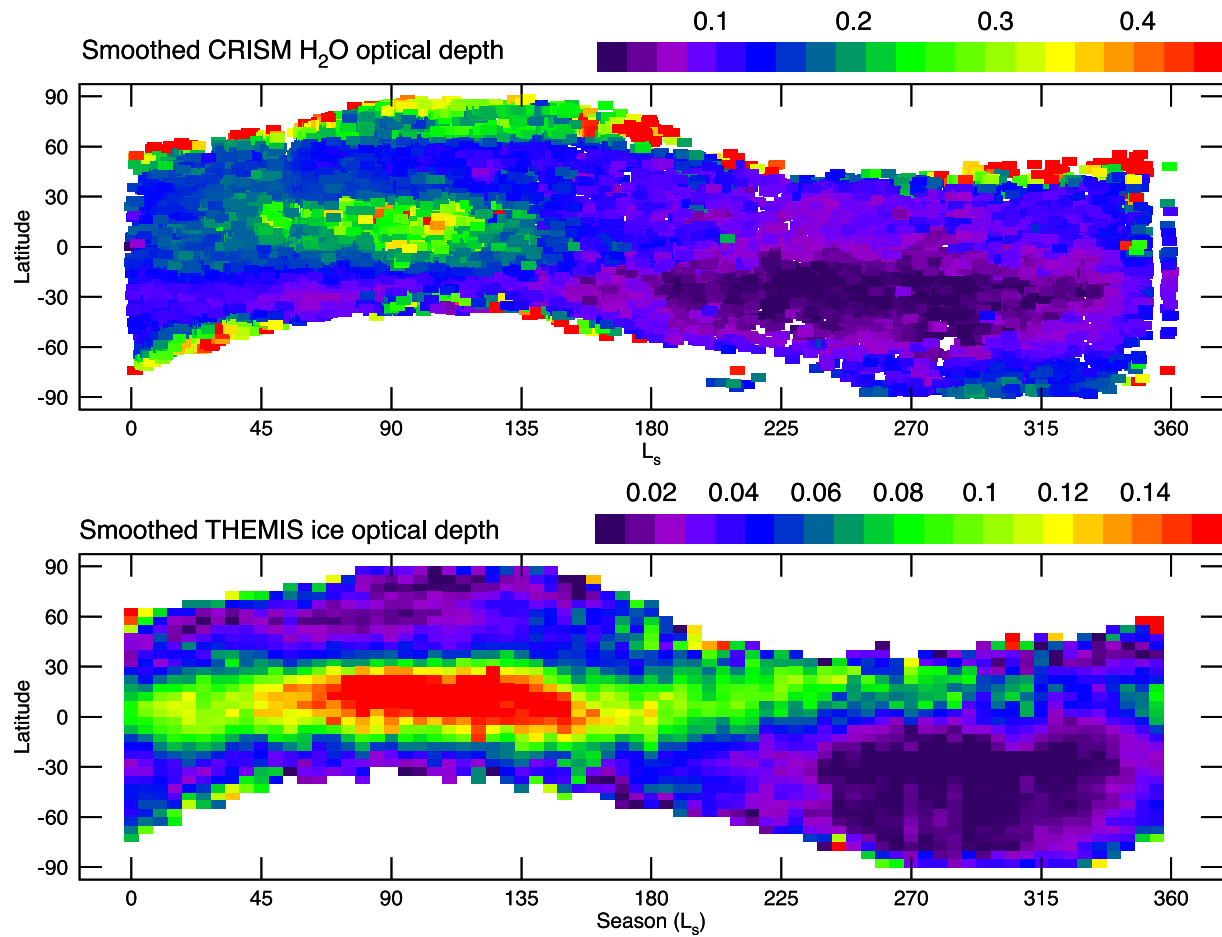
Figure 9. Zonal average of the water ice aerosol optical depth for over 5 Martian years. (top) Retrieved climatology of the Compact Reconnaissance Imaging Spectrometer for Mars water ice aerosol extinction (scattering and absorption) optical depth at ∼3.3 μm as a function of season (L_s) and latitude. The results are shown after applying a similar two-dimensional convolution of $\Delta L_s = 5°$ in the season dimension and Δlatitude = 5° in the latitudinal dimension.

$L_s = 250°$ and 290°, and is due to the increase in atmospheric temperatures caused by the global dust storm of MY 28, also observed by Smith (2009).

When comparing CRISM to THEMIS retrievals, the differences arising in the absolute values of optical depth can be attributed to the spectral ranges covered by the two instruments, the local time of the observations, and the retrieval methods.

The absorption optical depth for aerosols is one portion of the extinction (scattering + absorption) optical depth. For water ice aerosols, the extinction optical depth is 1.5 times the absorption optical depth at 825 cm^{-1} at the THEMIS wavelengths (Smith, 2004) or 1.4, as derived by Wolff and Clancy (2003). This ratio is wavelength dependent, and in order to convert the extinction optical depth from THEMIS (at 825 cm^{-1}) to CRISM (at 3.02 μm) wavelengths, an additional multiplication factor, $f_{ice} = 1.83$ is needed, as shown in the wavelength-dependent extinction coefficient in Figure 4, and derived by analyzing the scattering properties of water ice aerosols from TES and CRISM observations (e.g., Clancy et al., 2003; Wolff & Clancy, 2003; Wolff et al., 2009). The extinction optical depths from CRISM are therefore ∼2.7 times the absorption optical depths observed by THEMIS, explaining the color bar scales in Figures 8 and 9.

In addition to the differences caused by the wavelength regimes covered by CRISM and THEMIS, variations in the optical depth of the ACB also depend on the local time of the observations (e.g., Atwood et al., 2022; Smith, 2019b). The sun-synchronous orbit by MRO provides nadir observations by CRISM that are systematically at ∼15:00 local time. However, the Mars Odyssey mission conducted orbital maneuvers over the years to move the local time, hence allowing the study of local time variations in the water ice optical depth. The local

times covered by THEMIS during the MY 29−MY 30 and MY 31−MY 32 periods are ∼15:30 and 19:00, respectively. During these afternoon hours, there is a systematic increase in the water ice aerosol optical depth between 15:00 and 18:00, intensifying after 18:00 (Smith, 2019b), which explains the large seasonal and spatial extent of the ACB in the THEMIS retrievals beyond MY 31 as shown in Figure 8 (middle panel).

Extensive retrievals of daytime water ice optical depths during the aphelion season by EMIRS on-board the Emirates Mars Mission also strongly indicate large local time variations in optical depth, with significantly higher optical depth in the late afternoon hours after 18:00 as compared to 15:00 (Atwood et al., 2022). The unique observational coverage by EMIRS across the disk of Mars at nearly all latitudes and longitudes and at all local times is currently improving the analysis of daytime diurnal variability of cloud abundance. Atwood et al. (2022) conducted retrievals of water ice optical depths during daytime hours between 06:00 and 18:00 across all longitudes and latitudes between 30°S and 45°N during the aphelion same season, particularly between $L_s = 40°$ and 140°. When averaged over the aphelion season, the ACB had lower optical depth just after local noon, but higher optical depth values were observed in the morning and afternoon. Interestingly, the latitudinal extent of the ACB was found to extend northward of 30°N at some local times in contrast to being constrained between 10°S and 30°N when reported using spacecraft in sun-synchronous orbit pointing to the local mid-afternoon on the surface of the planet, corroborating the local-time driven difference in the spatial and seasonal extent of the ACB between CRISM and THEMIS beyond MY 31 as shown in Figure 8 (middle panel).

The retrieval methods differ between CRISM and THEMIS. THEMIS data include the 825 cm^{-1} water ice band, which being in the thermal infrared is only observable when sufficient thermal contrast exists between the surface and the atmosphere at the altitude at which water ice is present. However, CRISM retrievals are largely insensitive to temperature, and the spectral feature of water ice is due to the extinction of solar radiation reflected by the surface. To ensure sufficient thermal contrast, the THEMIS retrievals were restricted to observations over warm surfaces >220 K, and therefore retrievals over cold surfaces in the polar regions were excluded (e.g., Smith, 2019b; Smith et al., 2009). This is reflected in the THEMIS water ice aerosol climatology shown in Figure 9 (lower panel). Both CRISM and THEMIS climatologies are averaged over 5 Martian years and we smooth the results using a boxcar Kernel function of dimensions 5° L_s and 5° latitude in order to show the general trends in Figure 9. The insensitivity to surface temperature allowed the CRISM retrievals to cover cold surfaces (that were still in sunlight) and to detect high values in water ice optical depth from the north polar hood (Figure 9, upper panel). A general agreement is observed between both climatologies with respect to the timing in the maxima and minima in the optical depth. The seasonal and spatial pattern of the ACB, the portion of the north polar hood covering northern winter ($L_s = 270°–260°$) and spring ($L_s = 0°–90°$) seasons, the south polar hood covering the first half of the southern autumn ($L_s = 0°–45°$), mid-southern winter ($L_s \sim 135°$), and the seasons/locations severely lacking water ice aerosols ($L_s = 225°–350°$) are all in good agreement between the two climatologies.

A few exceptions include the presence of the north polar hood between mid-northern spring at $L_s = 70°$ and mid-northern summer at $L_s = 150°$ in the CRISM retrievals. The other exception is driven by the later local time covered by THEMIS during MY 31, 32, and MY 33, and is characterized by the presence of enhanced water ice aerosol optical depth extending from the equator at $L_s = 180°$ to latitudes north of 30°N at $L_s = 270°$.

Willame et al. (2017) provided retrievals of water ice aerosol optical depths for 4 Martian years between MY 27 and MY 30 using the SPICAM/UV instrument, with no indication of the local times covered by the observations. However, the seasonal and latitudinal distribution of the optical depth clearly showed the main features of the water ice aerosol climatology. Of particular interest is the presence of the polar hood during northern summer between $L_s = 90$ and 180° that we also detect in this work. This portion of the polar hood appeared every Martian year when successful retrievals were obtained (see Figure 7 in Willame et al., 2017). This enhancement in the total water ice column during northern summer and belonging to the north polar hood was also seen by OMEGA around $L_s = 130°$ (Olsen et al., 2021). To provide a visual overview of the principal features of the water ice aerosol climatology, Willame et al. (2017) combined the retrievals into one Martian year (see their Figure 8), showed elevated optical depths at polar latitudes in the north, starting as early as $L_s = 90°$, and indicated the presence of the north polar hood between $L_s = 90°$ and 180° that extended to low latitudes around 50°N at $L_s \sim 200°$ before lacking further coverage by SPICAM. The same pattern is well observed here in the retrieved CRISM climatology in Figures 8 and 9.

Figure 10 follows the seasonal variation of the water ice aerosol optical depth for the 5+ Martian years covered by the CRISM observations. The chosen latitudinal bin covers latitudes between 10°S and 30°N to capture the ACB.
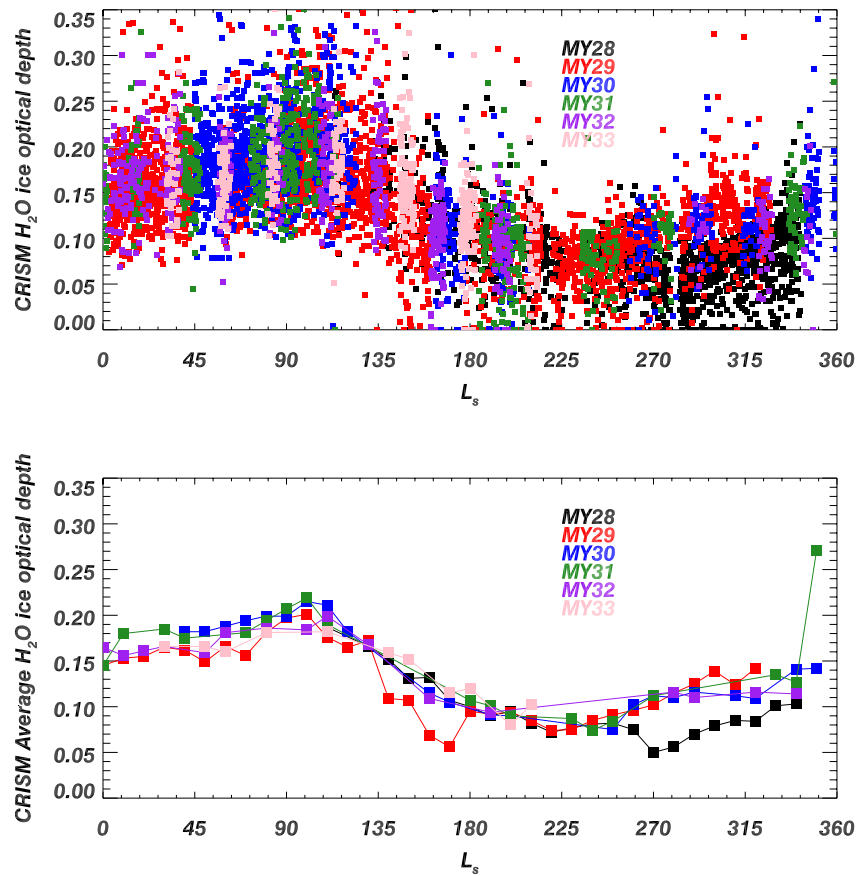
Figure 10. (top) Seasonal variation of the zonally averaged Compact Reconnaissance Imaging Spectrometer for Mars water ice aerosol optical depth for 5+ Martian year in the latitude bin 10°S to 30°N. The latitudes are chosen to capture the behavior of the aphelion cloud belt. (bottom) Same as the top panel but with an averaging of the optical depth using a seasonal bin of 10° in L_s to identify possible interannual variabilities.

The individual retrievals from every Martian year, when combined into one year and plotted over each other as shown in the top panel, indicate a similar pattern and range in water ice optical depth values, repeating itself every Martian year, except for MY 29 around $L_s = 145°$ and MY 28 beyond $L_s = 270°$ where lower ice aerosol optical depth is observed. The consistent increase in optical depth during northern summer is clearly observed, with a peak in optical depth around $L_s = 90°$, followed by a decline in optical depth, reaching its minimum during mid-southern spring around $L_s = 225°$ and indicating a lack of water ice aerosols. The period between mid-southern spring and southern summer ($L_s = 270°–360°$) is characterized by a modest rise in optical depth until the end of the Martian year.

To check for interannual variabilities, we averaged the optical depths from the top panel in Figure 10 using a seasonal bin of 10° in L_s and noticed the presence of lower optical depths in MY 28 during $L_s = 270°–315°$, which coincides with a global dust storm (July–August 2007; e.g., Smith, 2009) before going back to nominal levels. During this event, the warm atmosphere caused by the storm reduced the presence of water ice aerosols, therefore lowering the total column optical depth of water ice aerosols. The low optical depth in MY 29 between $L_s = 110°$ and 180° seen in Figure 10 is also observed in Figure 8 (lower panel) and is a byproduct of the small extent of the ACB that year. Willame et al. (2017) also retrieved low optical depth of water ice during the same period using OMEGA observations, in parallel with significantly high dust optical depth (see their Figure 7, top and middle panels). This similarly explains the decline in the water ice aerosol optical depth we detect here when an increased presence of dust warms the atmosphere and dissipates the clouds.

Figure 11 shows the latitudinal extension of the ACB as a function of longitude during the aphelion season using a L_s bin from 45° to 135°. Since the ACB is a generally repeated pattern, in order to improve the geographic coverage, the data from all the Martian years are combined into one map. The spatial variability is well observed, and is
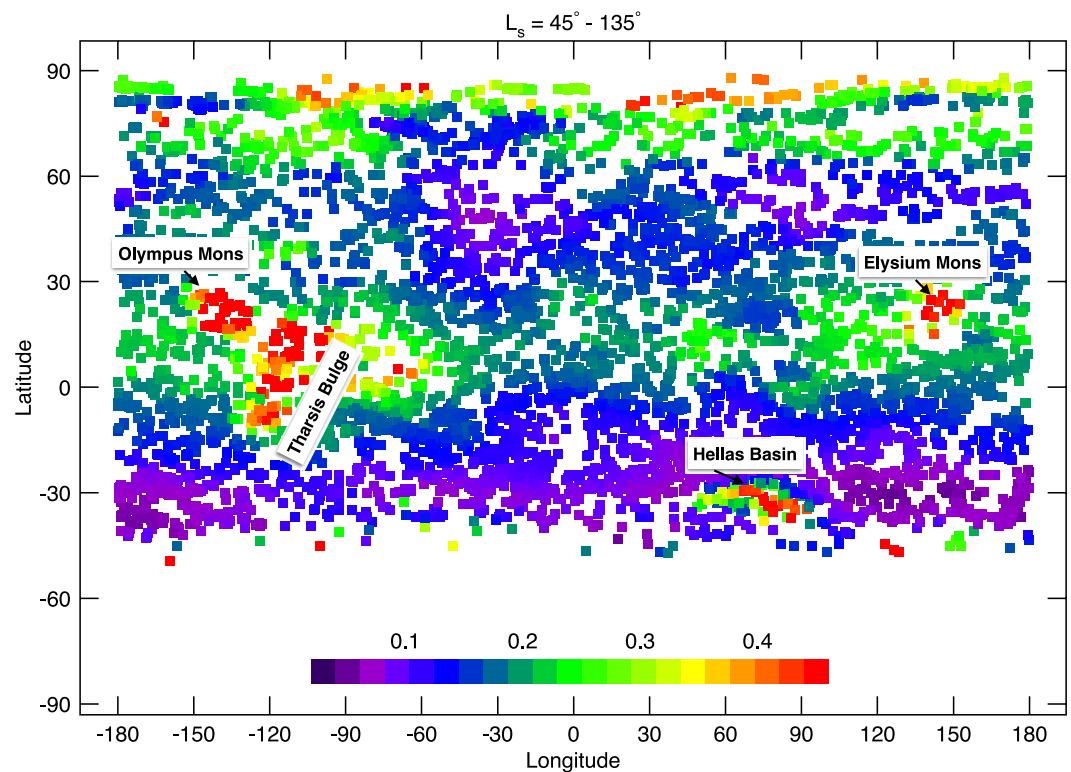
Figure 11. Retrieved Compact Reconnaissance Imaging Spectrometer for Mars water ice optical depth combined into one Martian year and averaged for the aphelion season between $L_s = 45°$ and $135°$ to display the geographic enhancement in optical depth inside the aphelion cloud belt. The results are convolved using a boxcar kernel with a $20° \times 5°$ longitude–latitude size.

consistent with previous reports (e.g., Atwood et al., 2022; Smith, 2004; Willame et al., 2017; Wolff et al., 2019), in particular around volcanoes where the adiabatic cooling originating from the upslope winds favors the formation of orographic clouds (Hartmann, 1978). Increased optical depths are observed over Elysium Mons (25°S, 147°E), Olympus Mons (20°N, 135°W) and the Tharsis bulge (center at 0°N, 115°W). High optical depths are also detected by CRISM over Hellas Basin (40°S, 70°E) as a result of the condensation of the water vapor that had originated from the north polar cap and traveled across the equator before mixing with the cold near-surface air inside the basin, as shown in Kahre et al. (2020).

5. Summary

Near infrared spectra returned by the CRISM spectrometer onboard MRO provide important information on the atmospheric constituents of the Martian atmosphere, including water vapor, carbon dioxide, carbon monoxide and the aerosol optical depth of water ice clouds. In this work, we use the daytime CRISM observations in the nadir pointing configuration, taken near 15:00 local time, and extending for over 5 Martian years between MY 28 at $L_s = 112°$ (27 September 2006) and MY 33 at $L_s = 213°$ (30 August 2016) to provide the first retrievals of the water ice cloud optical depth using the CRISM hyperspectral observations. We rely on the water ice aerosol feature near 3.3 μm to retrieve the optical depth. The resulting 22,000 successful retrievals well depict the main features of the water ice aerosol climatology with repeatable patterns every Martian year, except for MY 28 during the global dust storm and MY 29 when regional dust storms were observed.

The ACB is observed every Martian year at equatorial latitudes between 10°S and 30°N. Except for MY 29, the seasonal variation of the ACB indicates a repeatable pattern in water ice aerosol optical depth every Martian year, with peak values around the end of northern spring/beginning of northern summer ($L_s = 90°$), followed by a decline in optical depth continuing through mid-southern spring around $L_s = 225°$ during the dusty season and the warm atmosphere at equatorial latitudes.

The north polar hood is observed throughout northern spring and summer at latitudes poleward of 45°N every Martian year. The north polar hood reappears in northern winter beyond $L_s = 270°$ with an increasing optical depth compared to the previous seasons. A lack of water ice aerosols is repeatedly seen in the southern hemisphere throughout southern spring and summer between $L_s = 180°$ and 360°, reaching its largest geographic extent between 60°S and 0°S in the $L_s = 220°–270°$ range, and extending to mid-northern latitudes in MY 28 between $L_s = 220°$ and 270°.

The south polar hood is observed every Martian year in southern autumn between $L_s = 0°$ and 70°, where it reaches latitudes around 60°S, before re-emerging during southern winter between $L_s = 90°$ and $L_s = 180°$ at latitudes 45°S and 60°S, respectively, before dissipating in southern spring. The south polar hood is also seen during southern summer between $L_s = 270°$ and 360° for both MY 29 and MY 30.

By combining the retrievals from 5 Martian years to increase the geographic coverage in the longitude-latitude dimension, we present the water ice aerosol optical depth during the aphelion season ($L_s = 45°–135°$) and locate the higher optical depth over the volcanoes of Olympus Mons, Elysium, and the Tharsis bulge, as well over Hellas Basin where the condensation of water vapor after mixing with the cold near-surface air increases the water ice aerosol optical depth inside the Basin.

The climatology presented here covers the entire lifetime of the CRISM near-infrared observations providing a valuable addition to the body of retrievals characterizing the current Mars climatology.

Data Availability Statement

The CRISM data set used here is available on the PDS geosciences node (Murchie, 2006). The THEMIS retrievals are available on Mendeley (Smith, 2019a). The resulting climatology from this work is available on Mendeley (Khayat, 2023).

References

Almatroushi, H., AlMazmi, H., AlMheiri, N., AlShamsi, M., AlTunaiji, E., Badri, K., et al. (2021). Emirates Mars Mission characterization of Mars atmosphere and dynamics and processes. *Space Science Reviews*, *217*(8), 89. https://doi.org/10.1007/s11214-021-00851-6

Amiri, H. E. S., Brain, D., Sharaf, O., Withnell, P., McGrath, M., Alloghani, M., et al. (2022). The emirates Mars mission. *Space Science Reviews*, *218*(1), 4. https://doi.org/10.1007/s11214-021-00868-x

Appéré, T., Schmitt, B., Langevin, Y., Douté, S., Pommerol, A., Forget, F., et al. (2011). Winter and spring evolution of northern seasonal deposits on Mars from OMEGA on Mars Express. *Journal of Geophysical Research*, *116*(E5), E05001. https://doi.org/10.1029/2010je003762

Atwood, S. A., Smith, M. D., Badri, K., Edwards, C. S., Christensen, P. R., Wolff, M. J., et al. (2022). Diurnal variability in EMIRS daytime observations of water ice clouds during Mars aphelion-season. *Geophysical Research Letters*, *49*(15), e2022GL099654. https://doi.org/10.1029/2022GL099654

Berk, A., Bernstein, L. S., Anderson, G. P., Acharya, P., Robertson, D., Chetwynd, J., & Adler-Golden, S. (1998). MODTRAN cloud and multiple scattering upgrades with application to AVIRIS. *Remote Sensing of Environment*, *65*(3), 367–375. https://doi.org/10.1016/s0034-4257(98)00045-5

Bertaux, J. L., Korablev, O., Perrier, S., Quémerais, E., Montmessin, F., Leblanc, F., et al. (2006). SPICAM on Mars Express: Observing modes and overview of UV spectrometer data and scientific results. *Journal of Geophysical Research*, *111*(E10), E10S90. https://doi.org/10.1029/2006JE002690

Brown, A. J., Calvin, W. M., Becerra, P., & Byrne, S. (2016). Martian north polar cap summer water cycle. *Icarus*, *277*, 401–415. https://doi.org/10.1016/j.icarus.2016.05.007

Christensen, P. R., Bandfield, J. L., Hamilton, V. E., Ruff, S. W., Kieffer, H. H., Titus, T. N., et al. (2001). Mars Global surveyor thermal emission spectrometer experiment: Investigation description and surface science results. *Journal of Geophysical Research*, *106*(E10), 23823–23871. https://doi.org/10.1029/2000je001370

Clancy, R. T., Montmessin, F., Benson, J., Daerden, F., Colaprete, A., & Wolff, M. J. (2017). *Mars clouds. Chapter 5 in "The atmosphere and climate of Mars"*. Cambridge University Press. https://doi.org/10.1017/9781139060172.005

Clancy, R. T., Sandor, B., Wolff, M. J., Smith, M. D., Lefèvre, F., Madeleine, J. B., et al. (2012). Extensive MRO CRISM observations of 1.27 μm O_2 airglow in Mars polar night and their comparison to MRO MCS temperature profiles and LMD GCM simulations. *Journal of Geophysical Research*, *117*(E11), E00J10. https://doi.org/10.1029/2011JE004018

Clancy, R. T., Sandor, B. J., Wolff, M. J., Smith, M. D., Lefèvre, F., Madeleine, J. B., et al. (2013). Correction to "Extensive MRO CRISM observations of 1.27 μm O_2 airglow in Mars polar night and their comparison to MRO MCS temperature profiles and LMD GCM simulations". *Journal of Geophysical Research: Planets*, *118*(5), 1148–1154. https://doi.org/10.1002/jgre.20073

Clancy, R. T., Wolff, M. J., & Christensen, P. R. (2003). Mars aerosol studies with the MGS-TES emission phase function observations: Optical depths, particle sizes, and ice cloud types versus latitude and solar longitude. *Journal of Geophysical Research*, *108*(E9), 5098. https://doi.org/10.1029/2003JE002058

Curran, R. J., Conrath, B. J., Hanel, R. A., Kunde, V. G., & Pearl, J. C. (1973). Mars: Mariner 9 spectroscopic evidence for H_2O ice clouds. *Science*, *182*(4110), 381–383. https://doi.org/10.1126/science.182.4110.381

Edwards, C. S., Christensen, P. R., Mehall, G. L., Anwar, S., Tunaiji, E. A., Badri, K., et al. (2021). The Emirates Mars mission (EMM) Emirates Mars InfraRed spectrometer (EMIRS) instrument. *Space Science Reviews*, *217*(7), 77. https://doi.org/10.1007/s11214-021-00848-1

Fedorova, A., Montmessin, F., Korablev, O., Luginin, M., Trokhimovskiy, A., Belyaev, D. A., et al. (2020). Stormy water on Mars: The distribution and saturation of atmospheric water during the dusty season. *Science*, *367*(6475), 297–300. https://doi.org/10.1126/science.aay9522

Geminale, A., Grassi, D., Altieri, F., Serventi, G., Carli, C., Carrozzo, F. G., et al. (2015). Removal of atmospheric features in near infrared spectra by means of principal component analysis and target transformation on Mars: I. Method. *Icarus*, *253*, 51–65. https://doi.org/10.1016/j.icarus.2015.02.012

Guzewich, S. D., & Smith, M. D. (2019). Seasonal variation in Martian water ice cloud particle size. *Journal of Geophysical Research*, *124*(2), 636–643. https://doi.org/10.1029/2018je005843

Guzewich, S. D., Smith, M. D., & Wolff, M. J. (2014). The vertical distribution of Martian aerosol particle size. *Journal of Geophysical Research: Planets*, *119*(12), 2694–2708. https://doi.org/10.1002/2014JE004704

Hartmann, W. K. (1978). Mars: Topographic control of clouds, 1907–1973. *Icarus*, *33*(2), 380–387. https://doi.org/10.1016/0019-1035(78)90158-6

Kahre, M. A., Haberle, R. M., Hollingsworth, J. L., & Wolff, M. J. (2020). MARCI-Observed clouds in the Hellas Basin during northern hemisphere summer on Mars: Interpretation with the NASA/Ames Legacy Mars global climate model. *Icarus*, *338*, 113512. https://doi.org/10.1016/j.icarus.2019.113512

Khayat, A. S. J. (2023). The climatology of water ice aerosols in the Martian atmosphere as retrieved by MRO/CRISM. *Mendeley Data, v1*. https://doi.org/10.17632/xfhwcrs2p8.1

Khayat, A. S. J., Smith, M. D., & Guzewich, S. D. (2019). Understanding the water cycle above the north polar cap on Mars using MRO CRISM retrievals of water vapor. *Icarus*, *321*, 722–735. https://doi.org/10.1016/j.icarus.2018.12.024

Khayat, A. S. J., McConnochie, T., & Smith, M. D. (2022). The annual cycle of water vapor above Gale crater as retrieved by CRISM and compared to ChemCam passive sky spectroscopy. *Icarus*, *115136*, 115136. https://doi.org/10.1016/j.icarus.2022.115136

Khayat, A. S. J., Smith, M. D., & Guzewich, S. D. (2020). Detections of water vapor increase over the north polar troughs on Mars as observed by CRISM. *Geophysical Research Letters*, *47*(3), e2019GL086195. https://doi.org/10.1029/2019GL086195

Khayat, A. S. J., Villanueva, G. L., Smith, M. D., & Guzewich, S. D. (2019). IRTF/CSHELL mapping of atmospheric HDO, H$_2$O and D/H on Mars during northern summer. *Icarus*, *330*, 204–216. https://doi.org/10.1016/j.icarus.2019.04.007

Langevin, Y., Bibring, J.-P., Montmessin, F., Forget, F., Vincendon, M., Douté, S., et al. (2007). Observations of the south seasonal cap of Mars during recession in 2004–2006 by the OMEGA visible/near-infrared imaging spectrometer on board Mars Express. *Journal of Geophysical Research*, *112*(E8), E08S12. https://doi.org/10.1029/2006je002841

Liuzzi, G., Villanueva, G. L., Crismani, M. M. J., Smith, M. D., Mumma, M. J., Daerden, F., et al. (2020). Strong variability of Martian water ice clouds during dust storms revealed from ExoMars Trace Gas Orbiter/NOMAD. *Journal of Geophysical Research: Planets*, *124*(4), e2019JE006250. https://doi.org/10.1029/2019JE006250

Madeleine, J. B., Forget, F., Spiga, A., Wolff, M. J., Montmessin, F., Vincendon, M., et al. (2012). Aphelion water-ice cloud mapping and property retrieval using the OMEGA imaging spectrometer onboard Mars Express. *Journal of Geophysical Research*, *117*(E11), E00J07. https://doi.org/10.1029/2011JE003940

Malin, M. C., Calvin, W. M., Cantor, B. A., Clancy, R. T., Haberle, R. M., James, P. B., et al. (2008). Climate, weather, and north polar observations from the Mars reconnaissance orbiter Mars color imager. *Icarus*, *194*(2), 501–512. https://doi.org/10.1016/j.icarus.2007.10.016

Millour, E., Forget, F., Spiga, A., Colaitis, A., Navarro, T., Madeleine, J. B., et al. (2012). Mars climate database version 5. In *European planetary science congress, 23–28 Sep 2012, Madrid*.

Montmessin, F., Forget, F., Rannou, P., Cabane, M., & Haberle, R. M. (2004). Origin and role of water ice clouds in the Martian water cycle as inferred from a General Circulation Model. *Journal of Geophysical Research*, *105*, 4109–4121. https://doi.org/10.1029/2004JE002284

Murchie, S. (2006). MRO CRISM derived data record V1.0 [Dataset]. NASA Planetary Data System. https://doi.org/10.17189/1519567

Murchie, S., Arvidson, R., Bedini, P., Beisser, K., Bibring, J.-P., Bishop, J., et al. (2007). Compact reconnaissance imaging spectrometer for Mars (CRISM) on Mars reconnaissance orbiter (MRO). *Journal of Geophysical Research*, *112*(E11), E05S03. https://doi.org/10.1029/2006JE002682

Olsen, K. S., Forget, F., Madeleine, J.-B., Szantai, A., Audouard, J., Geminale, A., et al. (2021). Retrieval of the water ice column and physical properties of water-ice clouds in the Martian atmosphere using the OMEGA imaging spectrometer. *Icarus*, *353*, 113229. https://doi.org/10.1016/j.icarus.2019.03.006

Press, W. H., Teukolsky, S. A., Vetterling, W. T., & Flannery, B. P. (1992). *Numerical recipes in Fortran 77: The Art of scientific computing*. Cambridge University Press.

Smith, M. D. (2004). Interannual variability in TES atmospheric observations of Mars during 1999–2003. *Icarus*, *167*(1), 148–165. https://doi.org/10.1016/j.icarus.2003.09.010

Smith, M. D. (2009). THEMIS observations of Mars aerosol optical depth from 2002–2008. *Icarus*, *202*(2), 444–452. https://doi.org/10.1016/j.icarus.2009.03.027

Smith, M. D. (2019a). Data for: Local time variation of water ice clouds on Mars as observed by THEMIS. *Mendeley Data, V1*. https://doi.org/10.17632/c53w836bbk.1

Smith, M. D. (2019b). Local time variation of water ice clouds on Mars as observed by THEMIS. *Icarus*, *333*, 273–282. https://doi.org/10.1016/j.icarus.2019.06.009

Smith, M. D., Badri, K., Atwood, S. A., Edwards, C. S., Christensen, P. R., Wolff, M. J., et al. (2022). EMIRS observations of the aphelion-season Mars atmosphere. *Geophysical Research Letters*, *49*(15), e2022GL099636. https://doi.org/10.1029/2022GL099636

Smith, M. D., Bandfield, J. L., Christensen, P. R., & Richardson, M. I. (2003). Thermal Emission Imaging System (THEMIS) infrared observations of atmospheric dust and water ice cloud optical depth. *Journal of Geophysical Research*, *108*(E11), 5115. https://doi.org/10.1029/2003JE002115

Smith, M. D., Daerden, F., Neary, L., & Khayat, A. (2018). The climatology of carbon monoxide and water vapor on Mars as observed by CRISM and modeled by the GEM-Mars general circulation model. *Icarus*, *301*, 117–131. https://doi.org/10.1016/j.icarus.2017.09.027

Smith, M. D., Pearl, J., Conrath, B., Christensen, P., & Vondrak, R. (2001). One Martian year of atmospheric observations by the thermal emission spectrometer. *Geophysical Research Letters*, *28*(22), 4263–4266. https://doi.org/10.1029/2001GL013608

Smith, M. D., Wolff, M. J., Clancy, R. T., Kleinböhl, A., & Murchie, S. L. (2013). Vertical distribution of dust and water ice aerosols from CRISM limb-geometry observations. *Journal of Geophysical Research: Planets*, *118*(2), 321–334. https://doi.org/10.1002/jgre.20047

Smith, M. D., Wolff, M. J., Clancy, R. T., & Murchie, S. L. (2009). Compact Reconnaissance Imaging Spectrometer observations of water vapor and carbon monoxide. *Journal of Geophysical Research*, *114*, E00D03. https://doi.org/10.1029/2008JE003288

Stcherbinine, A., Montmessin, F., Vincendon, M., Wolff, M. J., Vals, M., Korablev, O., et al. (2022). A two Martian years survey of water ice clouds on Mars with ACS onboard TGO. *Journal of Geophysical Research: Planets*, *127*(12), e2022JE007502. https://doi.org/10.1029/2022JE007502

Szantai, A., Audouard, J., Forget, F., Olsen, K. S., Gondet, B., Millour, E., et al. (2021). Martian cloud climatology and life cycle extracted from Mars Express OMEGA spectral images. *Icarus*, *353*, 114101. https://doi.org/10.1016/j.icarus.2020.114101

Thomas, G. E., & Stamnes, K. (1999). *Radiative transfer in the atmosphere and ocean*. Cambridge University Press.

Toigo, A. D., Smith, M. D., Seelos, F. P., & Murchie, S. L. (2013). High spatial and temporal resolution sampling of Martian gas abundances from CRISM spectra. *Journal of Geophysical Research*, *118*(1), 89–104. https://doi.org/10.1029/2012je004147

Willame, Y., Vandaele, A. C., Depiesse, C., Lefèvre, F., Letocart, V., Gillotay, D., & Montmessin, F. (2017). Retrieving cloud, dust and ozone abundances in the Martian atmosphere using SPICAM/UV nadir spectra. *Planetary and Space Science*, *142*, 9–25. https://doi.org/10.1016/j.pss.2017.04.011

Wolff, M. J., & Clancy, R. T. (2003). Constraints on the size of Martian aerosols from Thermal Emission Spectrometer observations. *Journal of Geophysical Research*, *108*(E9), 5097. https://doi.org/10.1029/2003JE002057

Wolff, M. J., Clancy, R. T., Kahre, M. A., Haberle, R. M., Forget, F., Cantor, B. A., & Malin, M. C. (2019). Mapping water ice clouds on Mars with MRO/MARCI. *Icarus*, *332*, 24–49. https://doi.org/10.1016/j.icarus.2019.05.041

Wolff, M. J., Smith, M. D., Clancy, R. T., Arvidson, R., Kahre, M., Seelos, F., et al. (2009). Wavelength dependence of dust aerosol single scattering albedo as observed by the Compact Reconnaissance Imaging Spectrometer. *Journal of Geophysical Research*, *114*, E00D04. https://doi.org/10.1029/2009JE00350

Wolff, M. J., Smith, M. D., Clancy, R. T., Spanovich, N., Whitney, B. A., Lemmon, M. T., et al. (2006). Constraints on dust aerosols from the Mars Exploration Rovers using MGS overflights and Mini-TES. *Journal of Geophysical Research*, *111*(E12), E12S17. https://doi.org/10.1029/2006JE002786

Zurek, R. W., & Smrekar, S. E. (2007). An overview of the Mars Reconnaissance Orbiter (MRO) science mission. *Journal of Geophysical Research*, *112*(E5), E05S01. https://doi.org/10.1029/2006JE002701